

PAPER • OPEN ACCESS

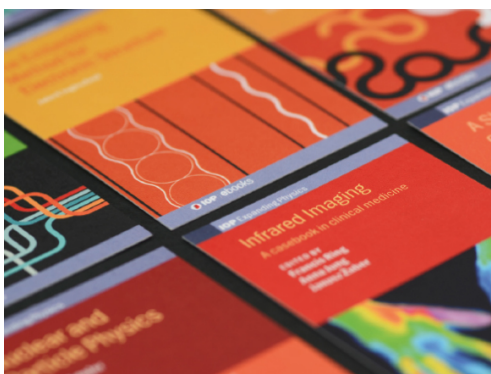
Development of control mechanisms for a laser wakefield accelerator-driven bremsstrahlung x-ray source for advanced radiographic imaging

To cite this article: C I D Underwood *et al* 2020 *Plasma Phys. Control. Fusion* **62** 124002

View the [article online](#) for updates and enhancements.

You may also like

- [Status of the Transverse Diagnostics at FLASHForward](#)
P Niknejadi, R D'Arcy, M C Kaluza *et al.*
- [2020 roadmap on plasma accelerators](#)
Félicie Albert, M E Couprie, Alexander Debus *et al.*
- [Parametric study of high-energy ring-shaped electron beams from a laser wakefield accelerator](#)
A Maitrallain, E Brunetti, M J V Streeter *et al.*













IOP | ebooks™

Bringing together innovative digital publishing with leading authors from the global scientific community.

Start exploring the collection—download the first chapter of every title for free.

Development of control mechanisms for a laser wakefield accelerator-driven bremsstrahlung x-ray source for advanced radiographic imaging

C I D Underwood^{1,9} , C D Baird^{1,2,9} , C D Murphy¹ , C D Armstrong² , C Thornton² , O J Finlay³, M J V Streeter⁴, M P Selwood¹ , N Brierley⁵, S Cipiccia⁶, J-N Gruse⁴ , P McKenna^{7,8} , Z Najmudin⁴ , D Neely^{2,7}, D Rusby², D R Symes² and C M Brenner² 

¹ York Plasma Institute, Department of Physics, University of York, York YO10 5DD, United Kingdom

² Central Laser Facility, STFC Rutherford Appleton Laboratory, Didcot OX11 0QX, United Kingdom

³ The Cockcroft Institute, Keckwick Lane, Daresbury, WA4 4AD, United Kingdom

⁴ The John Adams Institute for Accelerator Science, Imperial College London, London, SW7 2AZ, United Kingdom

⁵ The Manufacturing Technology Center, Ansty Park, Coventry, CV7 9JU, United Kingdom

⁶ Diamond Light Source, Harwell Science and Innovation Campus, Fermi Avenue, Didcot OX11 0DE, United Kingdom

⁷ SUPA, Department of Physics, University of Strathclyde, Glasgow, G4 0NG, United Kingdom

⁸ The Cockcroft Institute, Sci-Tech Daresbury, Warrington, WA4 4AD, United Kingdom

E-mail: christopher.underwood@york.ac.uk

Received 23 June 2020, revised 14 September 2020

Accepted for publication 6 October 2020

Published 29 October 2020



Abstract

A high power laser was used to accelerate electrons in a laser-driven wakefield accelerator. The high energy electrons were then used to generate an x-ray beam by passing them through a converter target. This bremsstrahlung source was characterised and used to perform penetrative imaging of industrially relevant samples. The photon spectrum had a critical energy in excess of 100 MeV and a source size smaller than the resolution of the diagnostic ($\lesssim 150 \mu\text{m}$).

Simulations indicate a significantly smaller source is achievable. Variations in the x-ray source characteristics were realised through changes to the plasma and converter parameters while simulations confirm the adaptability of the source. Imaging of high areal density objects with 150 μm resolution was performed, demonstrating the unique advantages of this novel source.

Keywords: laser wakefield acceleration, bremsstrahlung source, x-ray characterisation, radiography, non-destructive testing

(Some figures may appear in colour only in the online journal)

1. Introduction

High-power (TW), short-pulse (fs) lasers have been used in recent years to develop compact particle accelerators. A laser wakefield accelerator (LWFA) uses a laser-driven plasma waves to trap and accelerate electrons. Significant advances have been made since the LWFA was originally conceived by Tajima and Dawson [1], with experimental results

⁹ These authors contributed equally to this work.



Original Content from this work may be used under the terms of the [Creative Commons Attribution 4.0 licence](https://creativecommons.org/licenses/by/4.0/). Any further distribution of this work must maintain attribution to the author(s) and the title of the work, journal citation and DOI.

demonstrating high-quality electron beams with energies in the multi-GeV range [2], and energy spreads of $\lesssim 5\%$ [3, 4]. From these electron beams, there are several approaches to generating high-brightness, ultra-short pulse duration x-ray pulses. These include betatron oscillations [5, 6], inverse Compton scattering (ICS) [7], and bremsstrahlung radiation [8]. For x-ray production via betatron oscillations, the inherent transverse motion of the electrons in the wake generates x-ray radiation (10–100 keV) [5] which, due to its micron-scale source size and high-spatial coherence, is ideal for phase-contrast imaging [6, 9–12]. ICS, where the highly energetic electrons collide with a second laser pulse, is an effective way to produce MeV-scale, narrow energy spread x-rays [13, 14]. Such LWFA light sources have been studied extensively and reviewed by Corde *et al* [15] and Albert and Thomas [16].

Compact x-ray sources for imaging have also been demonstrated using bremsstrahlung radiation [8, 17–21], which is produced by the deceleration of charged particles in the nuclear field. Electrons incident on a high-Z material produce a cone of radiation with a broad energy spread extending up to the maximum electron energy. In applications for which high photon energy and flux is required for penetration of dense materials, a large divergence for wide field-of-view is required, and where a single-laser setup is desirable, bremsstrahlung sources have a distinct advantage over both betatron radiation and ICS sources. One potential application is *non-destructive testing* (NDT), where rapid high resolution (<0.1 mm) tomography of large, dense objects is of interest. A high flux, highly penetrative spectrum and small source size are required to image small features in high density samples. The most challenging objects in aerospace, automotive and nuclear sectors are additively manufactured structures with fine internal features composed of materials such as steel or nickel, which need to be inspected for failure indicators and quality control.

For x-ray NDT requiring photon energies >1 MeV the current industry standard approach is to use a linear accelerator (linac) to produce electrons, which are then converted to bremsstrahlung by interacting with a high-Z material. Commercial linac sources are often limited to source sizes in the millimetre range [22]. Direct laser-solid interaction bremsstrahlung sources can readily achieve multi-MeV energies with high flux and sub-millimetre source size, capable of penetrating even the densest materials [23]. The refluxing fields generated in the solid target work to increase the x-ray source size, although this may be overcome using a target with reduced lateral dimensions [24]. Small source sizes (~ 20 μm) [24] may be achieved using such targets, although the target must be replaced on each shot. The replacement and alignment of targets complicate the implementation of such systems at high repetition rate. Current solutions are reviewed by Principe *et al* [25]. Unlike x-ray sources from laser-solid interactions, the use of gas targetry for a LWFA means that the gas flow provides a new target after each shot without realignment of the laser. LWFAs have been shown to work at 5 Hz [26, 27] limited only by the laser repetition rate. Another advantage of a LWFA source is the decoupling of the electron and the photon production stages. The elimination of refluxing

electrons, creates inherently small source sizes (30 μm reported by Ben-Ismaïl *et al* [20]). The independent selection of the electron production (LWFA) and radiation target increases the adaptability of the x-ray source.

Here, results are presented of a recent experiment using the Gemini laser system at the Rutherford Appleton Laboratory [28], demonstrating the applicability of a LWFA bremsstrahlung source for high quality imaging of an additively manufactured Inconel (nickel-alloy) industrial test object. It is shown that x-ray emission can be tuned to image a range of objects with different material properties, by changing the electron beam properties or converter thickness and composition.

2. Experimental setup

The experimental setup is shown in figure 1. The south beam of the Gemini laser was focused using a $f/40$ parabolic mirror, delivering 6 ± 0.7 J of energy in 49 ± 3 fs. The focal spot was measured to be an ellipse with major and minor axes of $50 \mu\text{m} \times 40 \mu\text{m}$, giving a peak intensity of $(2.9 \pm 0.4) \times 10^{18} \text{ W cm}^{-2}$ ($a_0 \sim 1.2$). At the interaction point was a gas cell which was 11.8 mm in length. After passing through the gas cell, the laser pulse was diverted onto a laser beam dump by a thin polyimide tape acting as a plasma mirror. The accelerated electron bunch then propagated through a converter material mounted 50 mm behind the gas cell. After the converter there was a magnetic dipole spectrometer (total magnetic length $\int B(x)dx = 0.4 \text{ Tm}$), with the plane of deflection orthogonal to the laser polarisation. This was used to measure the electron spectrum with the second dimension of the spectrometer screen giving information about the divergence in the non-dispersive direction. When the bremsstrahlung converter was in place, this magnet prevented the electrons from irradiating the samples which would have otherwise generated a secondary bremsstrahlung source.

By varying the plasma density, through changing the gas cell inlet pressure, the properties of the electron bunch were changed. Pure helium was used to fill the gas cell. Changing the electron plasma density allowed the tuning of the total accelerated charge and the maximum electron energy. This enabled the bremsstrahlung source from the converter to be modified.

A range of samples were mounted in one of three positions of varying distance from the source, allowing the field of view, resolution and magnification (M) to be adjusted to the sample dimensions. Two sample positions were inside the vacuum chamber (370 mm from gas cell with $M = 10$ and 1560 mm from gas cell with $M = 2.5$), and the other outside (2600 mm from gas cell with $M = 1.6$). The attenuation of x-rays leaving the vacuum chamber was minimised by using a thin ($\sim 100 \mu\text{m}$) polyimide window. To perform x-ray imaging, a spatially-resolving scintillator, comprising a Cerium doped Lutetium based scintillation crystal (LYSO), was imaged with an optical CCD (charge-coupled device) camera. The experimental setup included the option for the imaging setup to be replaced with

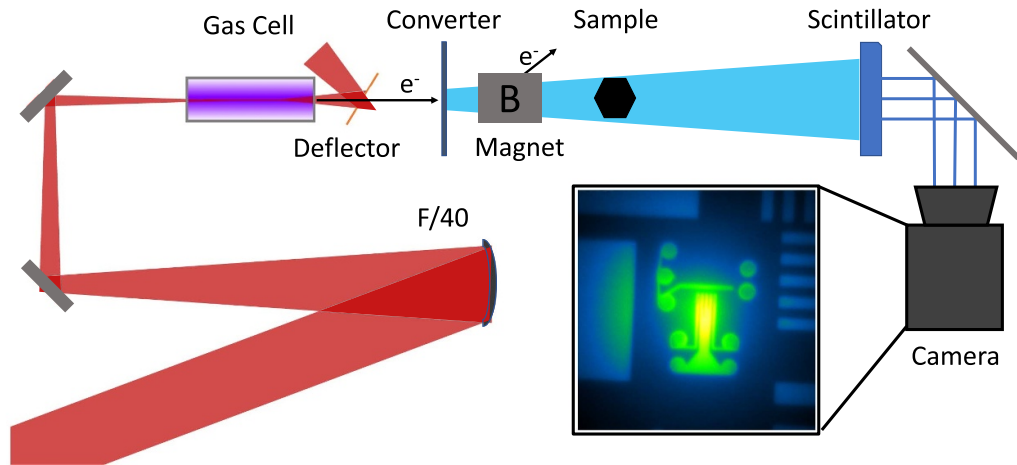


Figure 1. Schematic of the experiment showing the $f/40$ -focused laser accelerating electrons in the 11.8 mm gas cell. The laser was reflected after the cell, and the electron beam generated x-rays in the converter target. A magnet deflected the electron beam after the converter, and this was used as an electron spectrometer when the converter was removed. The x-rays project an image of the sample onto the scintillator.

a caesium iodide (CsI)-based diagnostic to characterise the x-ray beam. Both systems were located outside of the vacuum chamber.

2.1. x-ray diagnostic method

Spectrometry of high flux x-ray beams beyond 100 MeV remains a challenge, with limited options including Compton-scattering spectrometers [29], photonuclear activation measurements [30] and differential filtering [31]. In each case, the choice is based on experimental specifics and involves compromising on spatial or energy resolution, repetition rate, or a combination of all three. In our study, a differential self-filtering diagnostic was utilised, in order to retain sub-centimetre spatial resolution while obtaining some spectral information with a repetition rate higher than our laser shot rate (0.05 Hz). The specific detector had been fielded elsewhere [32, 33], demonstrating its suitability in the relevant energy range.

The x-ray beam was incident on a 47×33 array of scintillating CsI crystals, each $5 \text{ mm} \times 5 \text{ mm} \times 50 \text{ mm}$ in the geometry shown in figure 2. In this way, each subsequent column of crystals provides attenuation, thus providing spectral information. By viewing the array from the side, the x-ray beam divergence is imprinted on the vertical axis with spectral information obtained from the horizontal axis. The image is captured by the camera and shown in figures 2(a) and (b). This diagnostic is described in more detail by Behm *et al* [32].

To be able to deconvolve the detector response to return a photon spectrum, the response with respect to photons of a given energy is required. This response matrix was calculated using the Monte-Carlo toolkit Geant4 [34] by simulating the propagation of mono-energetic photon beams through the

detector and recording the simulated response. In extracting the photon spectrum, this detector has a non-uniqueness problem which must be overcome. To solve this issue, the spectrum is assumed to be of the form [32, 33]:

$$N_{\gamma}(E) = A * E^{-\frac{2}{3}} * \exp(-E/E_{\text{crit}}) \quad (1)$$

where $N_{\gamma}(E)$ is the number of photons at a given energy E , A is the amplitude constant, and E_{crit} defines the exponential slope. Due to the uncertainties in the data, confidence in the result is improved by repeating the fit multiple times (50x), each time adding a normal distributed value from the calibration error to each individual crystal. An average of the fits is used with the standard deviation as the error [35].

Figures 2(a) and (b) shows an example of the signal on the detector. The divergence angle of the beam is found from the full width half maximum of the signal in the first row of crystals which was 3500 mm from the interaction point. The total light emitted from the crystals is proportional to the total flux of the beam. Using the response curves of the detector the spectral information of the x-rays can be unfolded from the depth of the penetration.

Experimental calibration of the imaging of the CsI array was carried out using a thin ($100 \mu\text{m}$) aluminium foil converter that had little effect on the electron beam. This was evidenced experimentally, by recording no measurable increase in electron divergence on the spectrometer, and in simulations, which show less than 0.2% energy-loss in the electron beam. This meant that simultaneous measurements could be made of the electron spectrum and the CsI response. A comparison between simulation and experiment gave the correction factor per crystal.

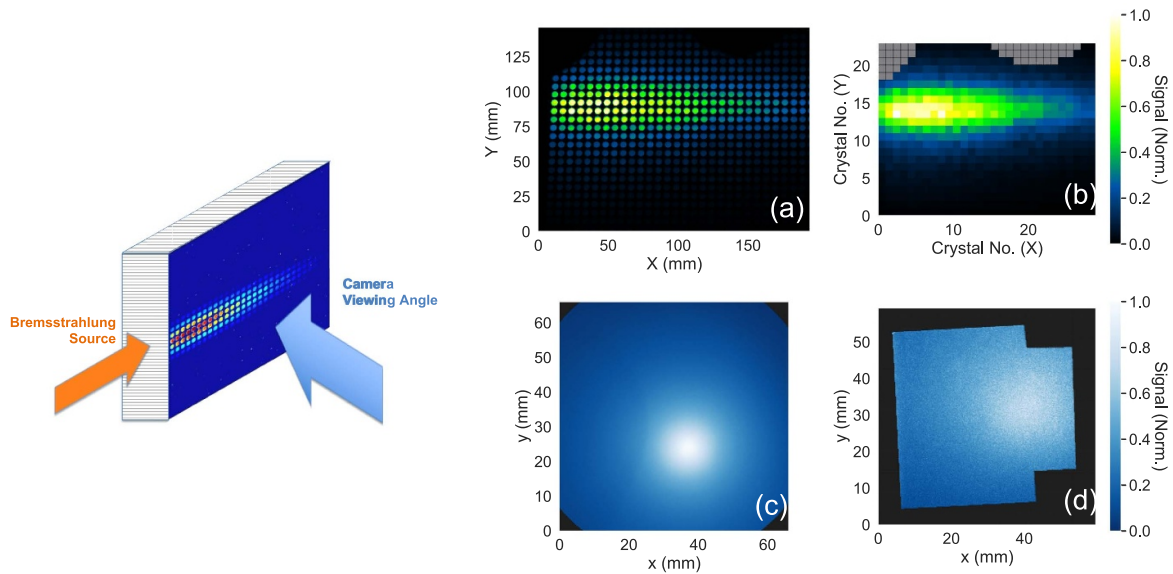


Figure 2. The left hand image shows the CsI scintillator x-ray diagnostic and the orientation of the photon flux to viewing angle. The right hand side show images of the different x-ray diagnostics. (a) The raw signal from the CsI array with the beam propagating through the detector from left to right; (b) Crystal values extracted from signal. The peak intensity occurs several crystals in due to the Compton scattering and pair production inside the detector; (c) 8 mm thick LYSO crystal ($r = 45$ mm); (d) 2 mm thick LYSO crystal (50 mm \times 50 mm).

The simulated spectrum of the x-rays was produced in Geant4 [34] using an ensemble of 10^7 electrons with the properties, energy spectrum and average divergence, of the average experimentally measured electrons for each of the three different plasma densities used. The simulations have an initial electron source size of $5 \mu\text{m}$, a normally distributed divergence with full width half maximum from table 1, and the distance from the electron source to the converter target was 2 cm. The energy of the simulated photons was collected by a detector that was positioned 100 mm behind the target in the model. The source size was determined in these simulations using penumbral imaging, where a sharp edge is imaged and the source size is calculated from the blurring of the edge [24]. The divergence was calculated from the full width half maximum of the signal.

3. Source characterisation

3.1. Electron beam

The electron spectrum was measured using a spectrometer with a energy of range from 100 MeV to 2 GeV. The mean electron beam properties at each plasma electron density (n_e), controlled by gas cell inlet pressure, is shown in figure 3. The maximum energy follows the inverse scaling estimate for maximum energy gain due to dephasing, $E_{\text{max}} = 2m_e c^2 n_c / n_e$ [36], shown in figure 3(b), where m_e is the rest mass of an electron, n_c is the critical plasma density. The data lies on the line when dephasing length (L_ϕ) of the electrons is shorter than the length of the gas cell, where $L_\phi \simeq (4/6\pi) \sqrt{a_0} \lambda_p (\omega_0 / \omega_p)^2$ [37], where λ_p is the plasma wavelength, ω_0 the frequency of the laser, ω_p the plasma frequency. The dashed navy line shows the point where L_ϕ is equal to the length of the gas

Table 1. The average divergence of the electron beams for the plasma density used.

Electron density	Divergence (mrad)
$3.6 \times 10^{18} \text{ cm}^{-3}$	2.7 ± 0.3
$5.4 \times 10^{18} \text{ cm}^{-3}$	2.6 ± 0.3
$7.2 \times 10^{18} \text{ cm}^{-3}$	4 ± 2

cell. By varying n_e between $3.6 \times 10^{18} \text{ cm}^{-3}$ and $9 \times 10^{18} \text{ cm}^{-3}$ the maximum energy was reduced from 850 ± 60 MeV to 370 ± 30 MeV.

In figure 3, shows that the maximum electron charge, and resulting x-ray flux, does not coincide with the lowest plasma density but at a higher density. This result is consistent with previous work including McGuffey *et al* [38] who explain this in terms of an increase in the available charge. The solid blue line on figure 3(c) shows the value of $\lambda_p / c\tau$ for the measured pulse duration. Above this density, the laser energy will be split between plasma wavelengths which is detrimental to the performance of the accelerator.

The average divergence, measured with the electron spectrometer, of the electron beam was used as the input for the Geant4 simulations, shown table 1. This is a 1D measurement of the divergence, meaning the electron beam profile could be elliptical. When the electron beam interacts with the laser pulse, either due to dephasing or a laser pulse longer than the plasma wavelength ($c\tau > \lambda_p$), the electron beam may become elliptical with the major axis in the direction of the laser polarisation [39]. The orientation of the electron spectrometer here means that the divergence measured would relate to the major axis of the ellipse, providing an upper-bound to the measurement.

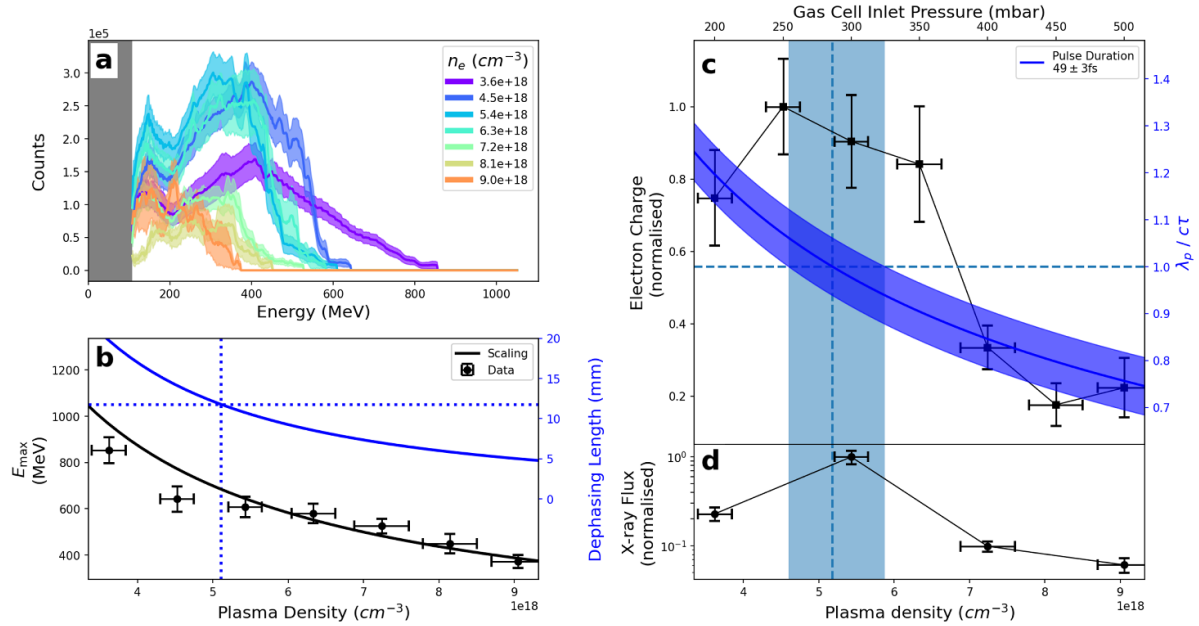


Figure 3. The measured source characteristics with respect to electron plasma density (n_e). (a) The average electron spectrum for the different plasma densities used. The shaded regions correspond to one standard error. (b) The maximum electron energy, showing that when the dephasing length (solid blue line) is shorter than the gas cell (dotted blue line) then the maximum energy follows the inverse scaling (solid black line). (c) Total electron charge (normalised) vs. n_e shown in black. The blue line represents $\lambda_p/c\tau$ for the measured pulse length of 49 ± 3 fs. The point where the pulse duration is matched to the plasma wavelength is shown (marked with the blue dashed line, and the shaded region the error in this value). (d) The x-ray flux (normalised) measured with the caesium iodide (CsI) array for the 1 mm iron converter target. The x-ray flux maximum corresponds to the electron beam with peak charge.

For this experiment the electrons were self-injected into the wake, as the gas was pure helium and the target a gas cell. Future work could use a controlled injection mechanism to improve the stability of the electron beams, such as ionisation injection [40], density profile injection [41] and dual laser pulses [42, 43]. These could be used to minimise the divergence, improving imaging quality by reducing the x-ray source size [44]. Additional consideration should be given to retaining the simplicity of the set-up since electron propagation distance must be small to minimise the source size.

3.2. x-ray beam

Using the experimental CsI x-ray diagnostic and Geant4 simulations, the source was characterised by measuring the flux, divergence and spectral properties. An upper limit on the source size was also inferred from the smallest feature on the resolution grid ($150 \mu\text{m}$) with simulations indicating the source size could be $\lesssim 50 \mu\text{m}$. The LWFA was operated at three different electron densities, 3.6 , 5.4 and $7.2 \times 10^{18} \text{cm}^{-3}$, to modify the electron spectrum. The bremsstrahlung converters were made of iron, aluminium or tantalum, and ranged in thickness from $100 \mu\text{m}$ to 10mm to further modify the x-ray characteristics. The simulations used the mean electron spectrum for each of the densities, shown in figure 3.

3.2.1. Divergence. Figure 4(a), shows that the smallest divergence was seen at $3.6 \times 10^{18} \text{cm}^{-3}$ and utilising the thinnest converters. The divergence angle of the x-rays increased

with n_e for two reasons. Firstly, the opening angle of the bremsstrahlung beam scales with $1/\gamma_e$ due to relativistic beaming [45] and γ_e decreases with increased plasma density, figures 3(a) and (b), where γ_e is the Lorentz factor of the electron beam. Secondly the experimentally measured divergence of the beam of electrons increased with plasma density, table 1. As the thickness of the converters tends to zero, the divergence of the photon source is dominated by that of the electrons. In both the experimental and simulation data, the $7.2 \times 10^{18} \text{cm}^{-3}$ plasma density shows a higher divergence for the thinnest converters, demonstrating this effect. The divergence of the x-rays increases with converter thickness, due to more scattering events occurring. For the electrons at higher plasma density, the simulations underestimate the divergence seen in the experiment. This is likely due to the lower γ_e electrons which are not measure, but more likely to be generated at higher plasma density.

A 2D Gaussian was fitted to the x-ray beam profiles for each of the different plasma densities, measured on the 8mm LYSO (figure 2(c)). Comparing the ratio of orthogonal axes of this fit gave a ratio of 1 ± 0.01 indicating that the beam is circular.

3.2.2. Spectrum. The increase in electron energy when operating at a lower plasma density, figure 3(b), results in an associated increase in the critical energy of the x-ray beam as demonstrated by figure 4(b). A lower E_{crit} is observed with increasing converter areal density (thickness \times density) due to the higher number of scattering events in the converter. After

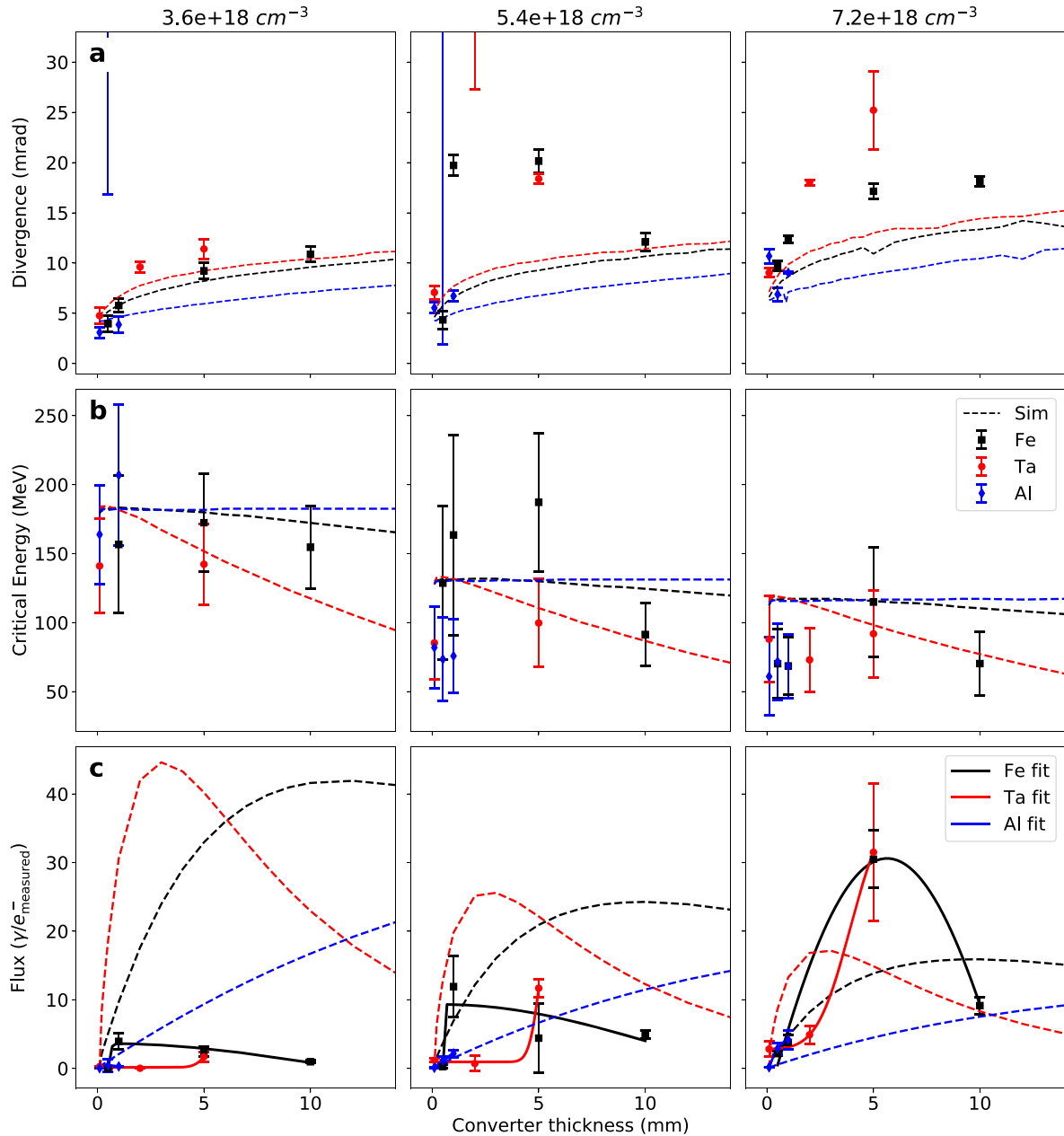


Figure 4. Effect of changing plasma density (n_e) on x-ray characteristics as measured by the CsI detector and inferred from simulations for the different converter materials used. Each column is a different n_e , and the legend is the same for all the subplots. The rows correspond to the different beam parameters. (a) Divergence showing that both an increase in electron divergence from the LWFA (table 1) and thickness of the converter increases the x-ray divergence. (b) Critical energy showing a decrease in critical energy with increasing converter thickness and increasing plasma density. Simulations show that the higher the atomic number of the converter material, the faster the critical energy of the beam decreases, supported experimentally by the thicker converters for tantalum showing a lower critical energy than the iron. (c) x-ray flux with the simulation showing a peak in the flux for the different converters. The data is shown normalised to the number of electrons measured. The differences between the simulation and experiment are likely from the electrons that were not measured experimentally (Electron spectrometer measured from 100 MeV up to 2 GeV). The experiment peak occurring for thinner converters again indicates the presence of unmeasured low energy electrons.

an emission event, the electron will have a lower energy, resulting in a lower energy radiation in subsequent events. Multiple scattering from a single electron in the production of more photons overall, increasing the flux of the source. The energies in these bremsstrahlung photon beams are higher than those measured previously using differential filtering (tens of MeV)

[46]. The change in E_{crit} due to variations in electron spectra was investigated. For the spectra recorded at $3.6 \times 10^{18} \text{ cm}^{-3}$, E_{crit} varied by $<10 \text{ MeV}$, whereas at $7.2 \times 10^{18} \text{ cm}^{-3}$ it was $\sim 20 \text{ MeV}$. The effect of the fluctuating electron beams for each density is less than the variation due to the increase in converter thickness.

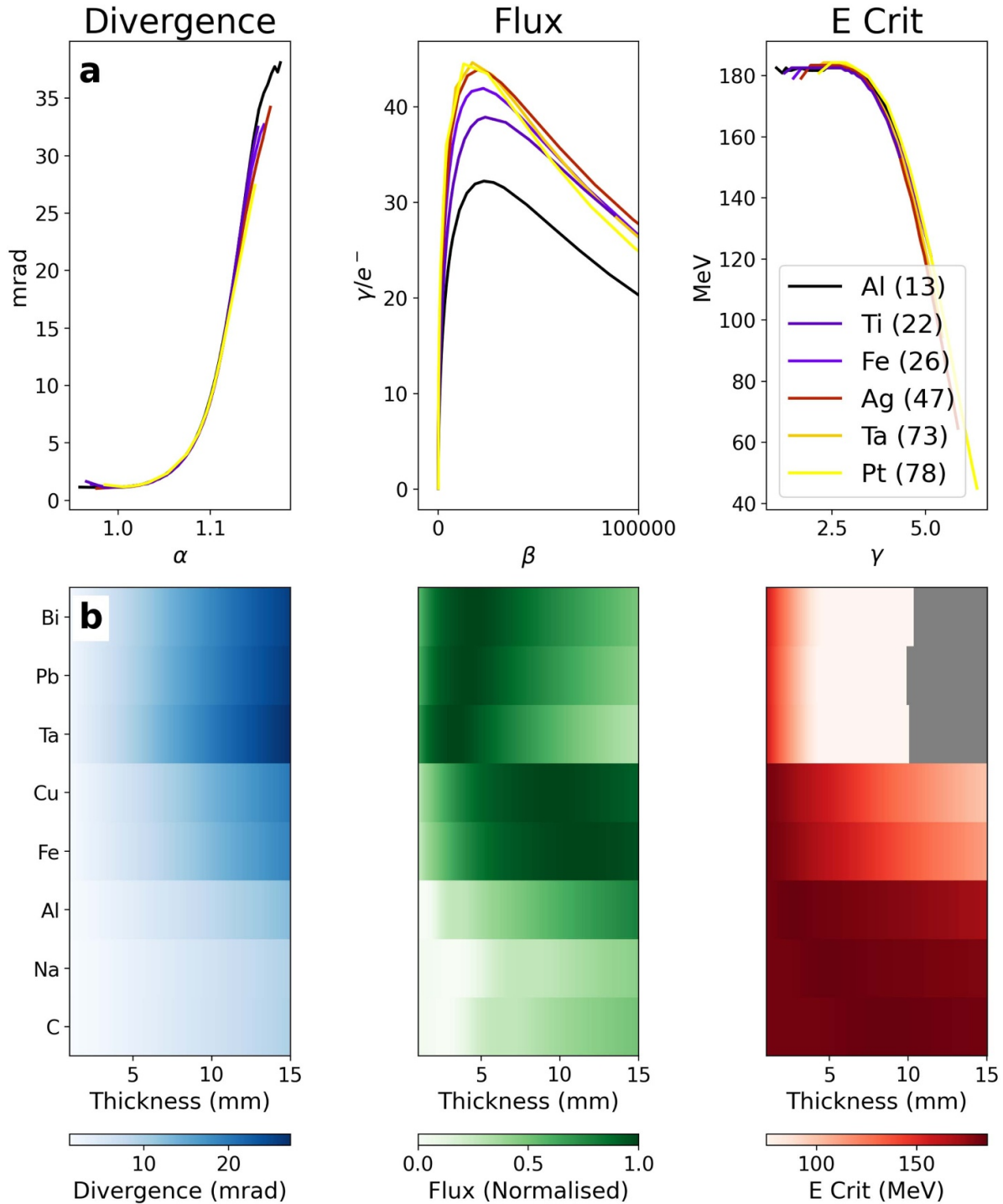


Figure 5. (a) Simulated x-ray source characteristics—divergence, flux and E_{crit} —demonstrating similarity of behaviour across materials. Each characteristic scales at different rates of thickness, density and nuclear charge (Z) as shown in equation (2). For divergence and E_{crit} the data from all the converter lies on the same line. The flux data also has an amplitude scaling with Z of the converter. To create the scaling axis the flux data was dividing by the peak height. (b) Demonstration of this control for a range of materials. (The grey region is outside the interpolation limits).

Therefore, by tuning the incident electron beam through changes in the plasma density, controlled by the gas cell pressure, and changing the converter material the spectral properties of the photons are altered. Spectral tuning is highly beneficial for optimising absorption contrast and decreasing noise in imaging, and allows the x-ray technology performance to be

matched to an individual object, thus increasing image acquisition efficiency.

3.2.3. Flux. Figures 3(c) and (d) demonstrates that the x-ray flux from a converter target (1 mm iron) is highest when

the accelerated electron charge is highest, in keeping with expectations. Figure 4(c) shows that the experimental data generally supports the simulation result showing that there is an optimal thickness in generating x-ray flux. Initially, an increase in thickness leads to an increase in photon flux. Further increase in thickness results in the material acting to absorb the radiation and so the x-ray flux decreases. The experimental measurement appears to peak at a smaller thickness (solid lines) compared to simulations (dashed lines). This may be understood as a consequence of the unmeasured electrons with energies of <100 MeV. The poorer agreement observed at the highest electron density may be attributed to the greater fluctuations in the electron spectrum. The variation in photon flux due to shot-to-shot fluctuations in the electron spectrum was also investigated. The photon flux varied by about a factor of 2 across the range of measured electron spectra. This is smaller than the change in flux demonstrated by the altering converter thickness in our experiment.

The result presented here agrees with previous work by S. Cipiccia *et al* [44] in terms of the divergence increasing with atomic number, Z . Agreement is also found in terms of flux increasing with both Z and thickness, R , up to a point. The reduction at the highest Z and R values correspond to studies of materials beyond the scope of the study of [44].

3.2.4. Source characteristic scalings. For broad utility of this source, and a given LWFA electron beam, the user may wish to select the area radiated, penetrative capability, and speed of acquisition to suit the specific application. This will require independent control of the divergence, critical energy and flux respectively. Simulating the source generated from an electron beam (the experimental electron spectrum taken at a plasma density of $3.6 \times 10^{18} \text{ cm}^{-3}$ for this data) shows the changes in the x-ray source which may result from changes in converter parameters. Figure 5(a) demonstrates the scaling of each characteristic by a unique combination of converter parameters: thickness (R); atomic number (Z); and density (ρ):

$$\begin{aligned}\alpha &= R^{0.03 \pm 0.01} \rho^{0.008 \pm 0.004} Z^{0.01 \pm 0.003} \\ \beta &= R^{1.63 \pm 0.02} \rho^{1.07 \pm 0.04} Z^{1.16 \pm 0.03} \\ \gamma &= R^{0.20 \pm 0.004} \rho^{0.29 \pm 0.002} Z^{0.08 \pm 0.001}\end{aligned}\quad (2)$$

where α , β and γ are the scaling parameters for divergence, flux, and critical energy, respectively. The scaling axes were found by minimising the difference between converters. The curves for divergence and critical energy are seen to only scale with this parameter, whereas the amplitude of the flux also increases with Z , so the data was normalised for the calculation.

Using the scaling axes, converters made of different materials can be evaluated, figure 5(b). The different properties scale with axis that are not parallel, which allows tuning of the different source properties with choice of material and thickness. For example a tantalum converter could produce a high flux,

low critical energy beam with a small divergence at a thickness of 3 mm, whereas using a thick converter of a lower atomic number material such as aluminium would allow a source with a higher critical energy to be produced with similar divergence.

4. Imaging quality

To enable high repetition rate x-ray radiography a LYSO crystal was placed in the beam with the scintillation light imaged onto a CCD camera. A typical beam profile in the LYSO configuration is shown in figures 2(c) and (d).

To quantify the imaging capability of the source, a 5 mm thick tungsten resolution grid was illuminated with the x-ray beam. To compare high- and lower-repetition rate detectors, the resulting shadow was projected onto 2 and 8 mm thick LYSO crystals, and Fujifilm BAS-TR image plate. The object and detectors were positioned to provide a magnification of 2.5 and the image plate was scanned with a FLA-5000 scanner. The radiograph generated in the thinner crystal shows a contrast of $21 \pm 4\%$ on $150 \mu\text{m}$ features as shown in figure 6. The light level in this image was low. The thicker crystal, while generating a brighter signal, resulted in significant blurring. The contrast is quantified, defined in terms of the pixel values I , as follows: Contrast = $(I_{\text{max}} - I_{\text{min}})/(I_{\text{max}} + I_{\text{min}})$. Measurements of $200 \mu\text{m}$ features with the 8 mm crystal had a contrast of $2 \pm 1\%$. Measurements of the same features with the image plate are shown in figure 7, with the contrast of the features found to be $67 \pm 4\%$.

These images show an experimental source size of $\lesssim 150 \mu\text{m}$ was achieved, and the measurement was detector limited. The small source size is possible due to the decoupling of the creation of electron and the generation of the x-rays by using a LWFA. The simulated source size scales with electron beam divergence, as this increases the area of the electron beam on the converter in agreement with S. Cipiccia *et al* [44]. Simulations show a source size of $\lesssim 50 \mu\text{m}$ for the thinnest converters at all plasma densities. Increasing the converter thickness, does increase the source size, but only up to a limit of around $100 \mu\text{m}$ for 3.6 and $5.4 \times 10^{18} \text{ cm}^{-3}$, and $140 \mu\text{m}$ for $7.2 \times 10^{18} \text{ cm}^{-3}$. The plateau in source size is a somewhat surprising result and so was investigated through additional simulations. These show that an increase in source size is due to electrons which scatter small angles, so that subsequent events still reach the detector, figure 8. If these scattering events are in the small angle limit ($\theta_i \rightarrow 0$), the source size is not increased significantly, but the divergence increases linearly with number of scattering events. If the first scattering event is into a large angle, θ_1 , (increasing the divergence of the source) the second scattering event will only contribute to an increase in the source size if the second photon produced by this electron strikes the detector. That is, $\theta_2 \sim \theta_1$. The chance of this becomes vanishingly small as the first scatter angle increases as the detector subtends a smaller azimuthal angle as the required polar angle increases, figure 8. The preservation of source size is, in a sense, empirical since it results from

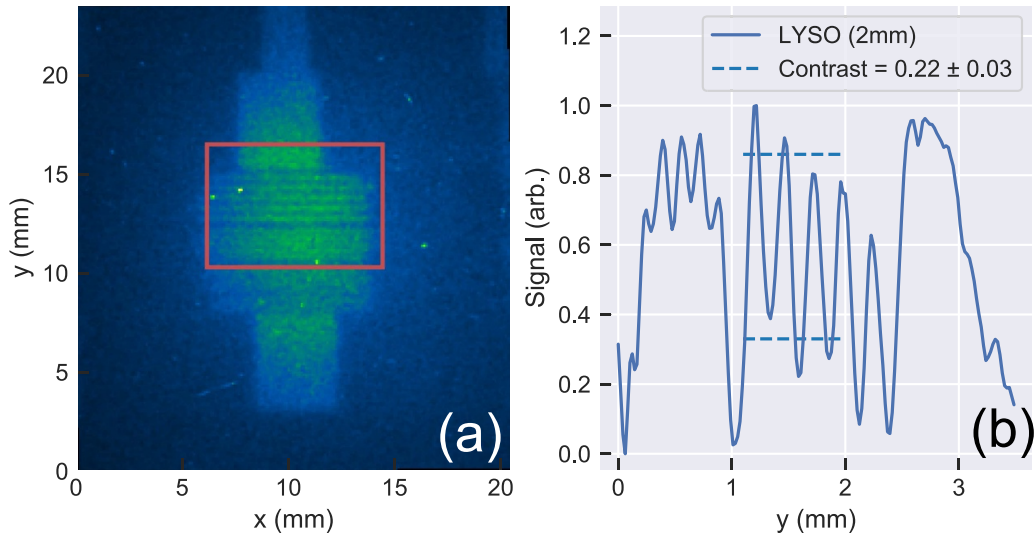


Figure 6. (a) Single shot image of small ($150\ \mu\text{m}$) features on by 2 mm LYSO. (b) A contrast of 0.22 ± 0.03 was measured for a line-out perpendicular to the features in the highlighted region.

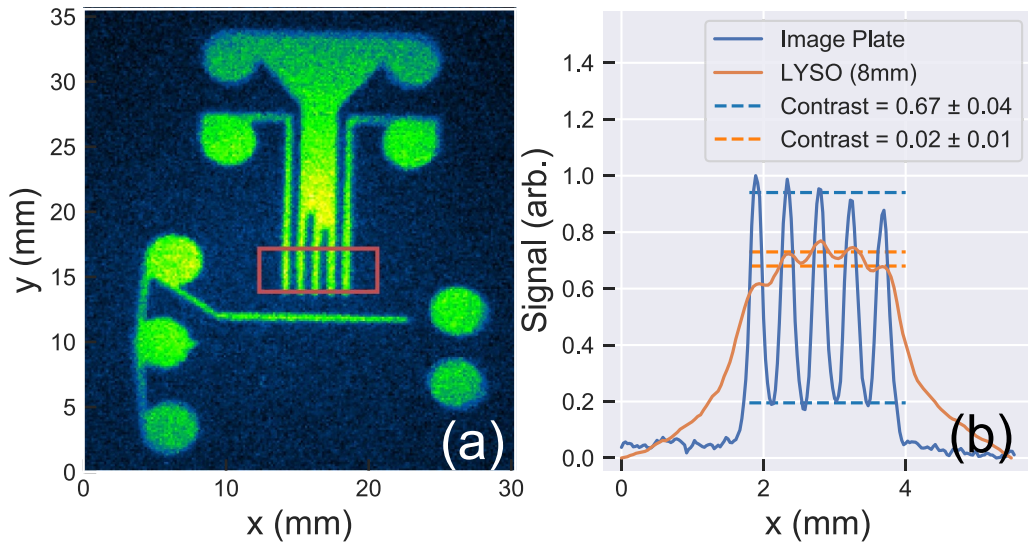


Figure 7. (a) Ten shot image plate scan of resolution grid. Features in the red box are $200\ \mu\text{m}$. (b) Contrast of a perpendicular line-out to the $200\ \mu\text{m}$ features shown in (a), as measured with image plate, and 8 mm thick LYSO. The scintillator material causes significant blurring due to its thickness.

the detector being a finite distance away (10 cm for simulations, 3.5 m for experiment). Therefore, increasing the thickness, and thus areal density, does not lead to an increase in the effective source size as the additionally generated photons do not contribute to the final image. This will also contribute to the reduction in flux as the areal density increases.

The different detectors have different abilities to image photons of different energies. For the image plate the response will be dominated by photons in the keV [47], whereas the LYSO scintillator will be able to detect photons up to the MeV range [48]. Experimentally the significant difference in the contrast between the detector types (image plate, 8 and 2 mm LYSO) demonstrates that the imaging quality in our setup is limited by the detector itself, and not by the source size. Therefore, the experimental source was $\lesssim 150\ \mu\text{m}$. High repetition

rate detectors of multi MeVs will have to be improved to capitalise fully on the resolution offered by these sources. Optics for imaging high energy ($>1\ \text{MeV}$) are currently being developed [49].

4.1. Sample imaging

To test the imaging capability of the source a variety of samples were used, provided by industrial collaborators. Figure 9(a) shows one example, an additively-manufactured star-based prism artefact composed of the nickel alloy Inconel718 which is around 5 cm in each dimension. This was placed outside the target chamber ($M = 1.6$), and imaged using bremsstrahlung from a 2 mm tantalum converter.

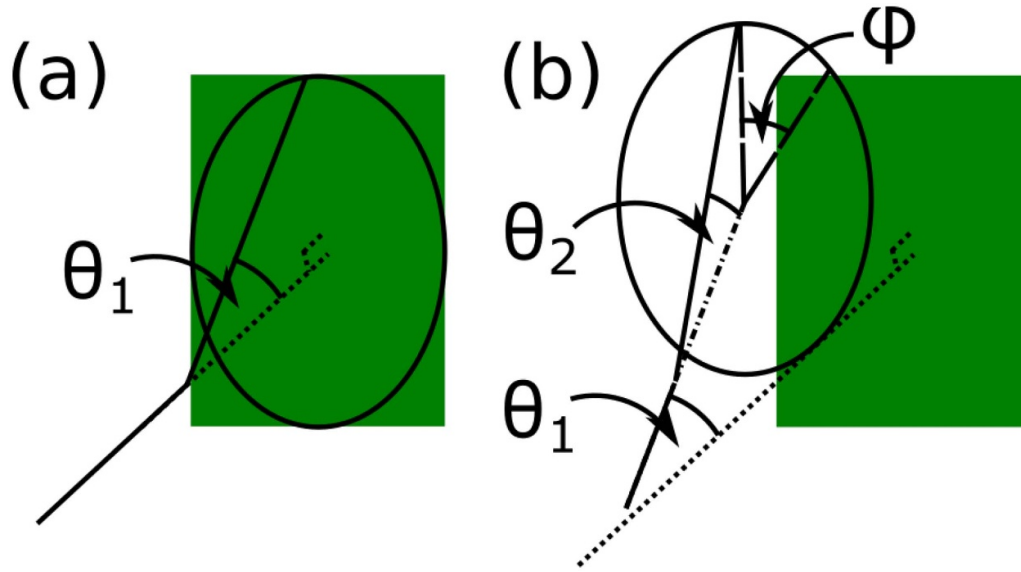


Figure 8. Schematic showing whether an emission event reaches the detector. (a) An on-axis event has a maximum acceptance angle θ_1 for a given detector. (b) For a scattering event from an off-axis electron for a given θ_2 there is only a small range of ϕ that subtends the detector.

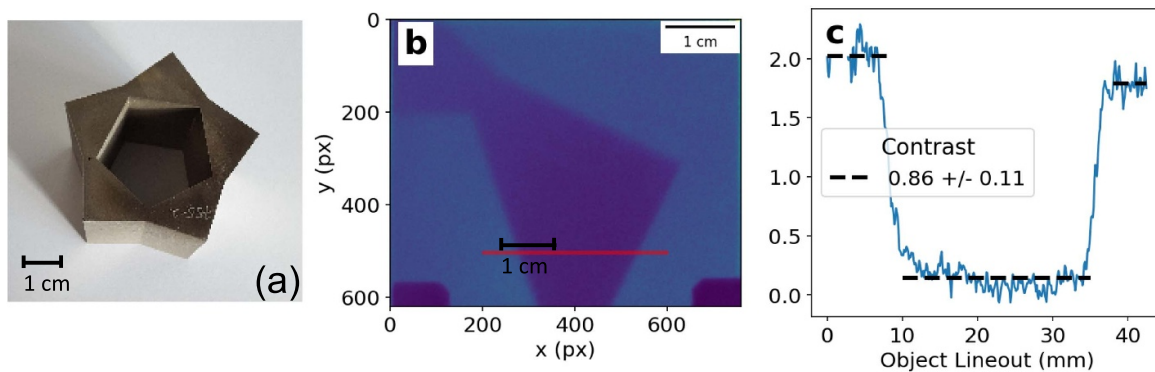


Figure 9. (a) Photograph of Inconel star object. (b) 2 mm LYSO image of star. The x-ray beam profile has been removed, and the image is the result of a pixel-wise median of 10 shots. (c) Contrast of 0.9 ± 0.1 of Inconel star object measured on the 2 mm LYSO for lineout marked on (b).

Figure 9(b) shows the shadow of the object projected onto 2 mm LYSO, where the scintillation light is collected by a CCD camera as shown in figure 1. The use of the thinner scintillator allows higher spatial resolution (due to reduced optical blurring) but also results in the image being dominated by lower energy x-rays. This also results in a larger field of view since the highest energy bremsstrahlung emission appears closest to the axis (in agreement with [50]) as apparent when comparing figures 2(c) and (d) as the thicker crystal will absorb more high energy photons [51]. Figure 9(c) shows a contrast of 0.9 ± 0.1 across the lineout indicated in figure 9(b) where the object is 5 cm thick Inconel (areal density 45 g cm^{-3}). The incomplete obscuration of the x-ray beam demonstrates the penetrative ability of the source. The attenuation coefficient for nickel for 10 MeV photons is $\sim 0.03/\text{cm}$, but for 0.1 MeV photons is $\sim 0.44/\text{cm}$ [52], so penetration of the sample is expected for the highest energy component of our source.

Figure 10 shows side projections of the star, imaged with an 8 mm LYSO crystal demonstrating the wide field of view of the x-ray beam. The acquisition of multiple projections demonstrates the potential to use the laser-driven source for tomographic reconstruction of industrial objects.

5. Summary

Using laser wakefield accelerated electrons and converter targets, a bremsstrahlung x-ray source was produced capable of imaging of high-density, industrially relevant materials with a resolution of $\lesssim 150 \mu\text{m}$, currently limited by the detector. This is significantly better than the industry-standard of $\sim 1 \text{ mm}$. By varying the electron density (through changing the inlet pressure of the gas target) or the converter, it has been shown, both experimentally and in simulation, that it is possible to control the brightness, divergence, and the characteristic energy of the

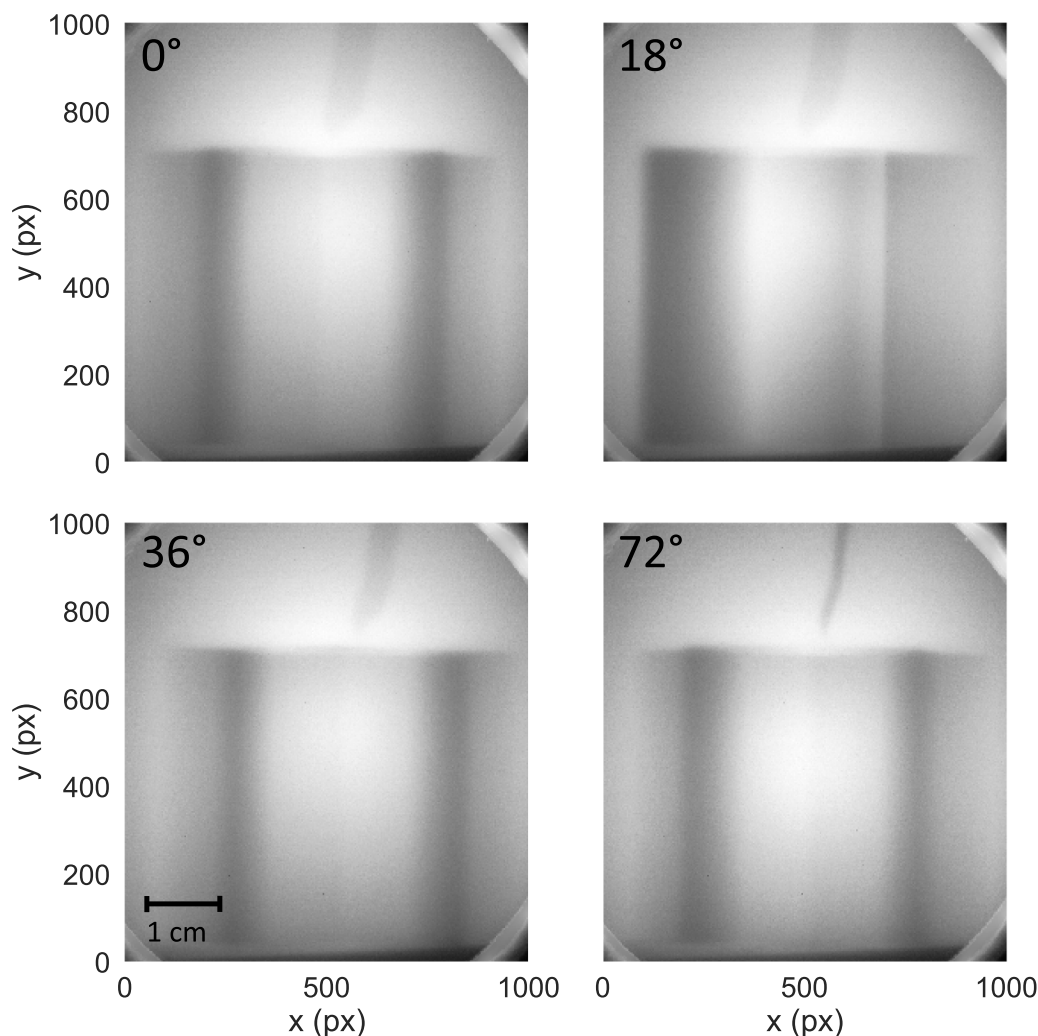


Figure 10. 8 mm LYSO images of nickel alloy star, image shown in figure 9, at various angular orientations, showing potential for tomographic reconstruction. The feature at the top of each image is a lead fiducial. Each image is the result of a pixel-wise median of 10 shots.

x-ray beam. The choice of converter includes thickness, density and the atomic number of the material. This laser produced source can provide a compact instrument for imaging of high areal density large objects and has the potential to become a valuable inspection tool in manufacturing. The detectors demonstrated here are capable of matching—and exceeding—the repetition rate of current laser systems, demonstrating a route to rapid tomographic imaging. High repetition rate (10 Hz) PW laser facilities are now opening up (ELI Beamlines [53], ELI-ALPS [54], EPAC [55]) and therefore, realisation of rapid high resolution MeV tomography for impact in high value manufacturing sectors is fast approaching.

Acknowledgments

The authors thank the staff at the Central Laser Facility and acknowledge funding from STFC (Grant Numbers ST/P002056/1 and ST/P002021/1), Engineering and Physical Sciences Research Council (Grant Number EP/L01663X/1) and AWE for their support of this work. We thank the Manufacturing Technology Centre for providing the Inconel

sample generated as part of the international standard efforts in ISO/ASTM 52905 led by Ben Dutton.

ORCID iDs

C I D Underwood [id https://orcid.org/0000-0002-1691-6377](https://orcid.org/0000-0002-1691-6377)
 C D Baird [id https://orcid.org/0000-0001-9973-7173](https://orcid.org/0000-0001-9973-7173)
 C D Murphy [id https://orcid.org/0000-0003-3849-3229](https://orcid.org/0000-0003-3849-3229)
 C D Armstrong [id https://orcid.org/0000-0003-2083-8487](https://orcid.org/0000-0003-2083-8487)
 C Thornton [id https://orcid.org/0000-0003-1267-5788](https://orcid.org/0000-0003-1267-5788)
 M P Selwood [id https://orcid.org/0000-0002-9163-1857](https://orcid.org/0000-0002-9163-1857)
 J-N Gruse [id https://orcid.org/0000-0002-4099-8341](https://orcid.org/0000-0002-4099-8341)
 P McKenna [id https://orcid.org/0000-0001-8061-7091](https://orcid.org/0000-0001-8061-7091)
 Z Najmudin [id https://orcid.org/0000-0001-6323-4005](https://orcid.org/0000-0001-6323-4005)
 C M Brenner [id https://orcid.org/0000-0003-0347-4415](https://orcid.org/0000-0003-0347-4415)

References

- [1] Tajima T and Dawson J M 1979 Laser electron accelerator *Phys. Rev. Lett.* **43** 267–70

- [2] Downer M C *et al* 2018 Diagnostics for plasma-based electron accelerators *Rev. Mod. Phys.* **90** 35002
- [3] Mangles S P D *et al* 2004 Monoenergetic beams of relativistic electrons from intense laser-plasma interactions *Nature* **431** 535–8
- [4] Geddes C G R *et al* 2016 High energy, low energy spread electron bunches produced via colliding pulse injection *AIP Conf. Proc.* **1777** 040003
- [5] Rouse A *et al* 2004 Production of a keV x-ray beam from synchrotron radiation in relativistic laser-plasma interaction *Phys. Rev. Lett.* **93** 1–4
- [6] Kneip S *et al* 2011 x-ray phase contrast imaging of biological specimens with femtosecond pulses of betatron radiation from a compact laser plasma wakefield accelerator *Appl. Phys. Lett.* **99** 1–4
- [7] Ta Phuoc K *et al* 2012 All-optical Compton gamma-ray source *Nat. Photon.* **6** 1–4
- [8] Glinec Y *et al* 2005 High-resolution γ -ray radiography produced by a laser-plasma driven electron source *Phys. Rev. Lett.* **94** 025003
- [9] Fourmaux S *et al* 2011 Single shot phase contrast imaging using laser-produced Betatron x-ray beam *Opt. Lett.* **36** 2426–8
- [10] Wenz J *et al* 2015 Quantitative x-ray phase-contrast microtomography from a compact laser-driven betatron source *Nat. Commun.* **6** 1–6
- [11] Hussein A E *et al* 2019 Laser-wakefield accelerators for high-resolution x-ray imaging of complex microstructures *Sci. Rep.* **9** 3249
- [12] Gruse J N *et al* 2020 Application of compact laser-driven accelerator x-ray sources for industrial imaging *Nucl. Instrum. Methods Phys. Res. A* **983** 164369
- [13] Chen S *et al* 2013 MeV-energy x rays from inverse Compton scattering with laser-wakefield accelerated electrons *Phys. Rev. Lett.* **110** 155003
- [14] Powers N D *et al* 2013 Quasi-monoenergetic and tunable x-rays from a laser-driven Compton light source *Nat. Photon.* **8** 28–31
- [15] Corde S *et al* 2013 Femtosecond x rays from laser-plasma accelerator *Rev. Mod. Phys.* **85** 1
- [16] Albert F and Thomas A G R 2016 Applications of laser wakefield accelerator-based light sources *Plasma Phys. Control. Fusion* **58** 103001
- [17] Edwards R D *et al* 2002 Characterization of a gamma-ray source based on a laser-plasma accelerator with applications to radiography *Appl. Phys. Lett.* **80** 2129–31
- [18] Döpp A *et al* 2016 A bremsstrahlung gamma-ray source based on stable ionization injection of electrons into a laser wakefield accelerator *Nucl. Instrum. Methods Phys. Res. A* **830** 515–19
- [19] Dong K *et al* 2018 Micro-spot gamma-ray generation based on laser wakefield acceleration *J. Appl. Phys.* **123** 243301
- [20] Ben-Ismaïl A *et al* 2011 Compact and high-quality gamma-ray source applied to 10 μm -range resolution radiography *Appl. Phys. Lett.* **98** 98–101
- [21] Wu Y *et al* 2018 Towards high-energy, high-resolution computed tomography via a laser driven micro-spot gamma-ray source *Sci. Rep.* **8** 1–7
- [22] Varex Imaging 2019 (www.vareximaging.com/products/security-industrial/linear-accelerators)
- [23] Brenner C *et al* 2015 Laser-driven x-ray and neutron source development for industrial applications of plasma accelerators *Plasma Phys. Control. Fusion* **58** 014039
- [24] Armstrong C D *et al* 2019 Bremsstrahlung emission from high power laser interactions with constrained targets for industrial radiography *High Power Laser Sci. Eng.* **7** 21–3
- [25] Prencipe I *et al* 2017 Targets for high repetition rate laser facilities: needs, challenges and perspectives *High Power Laser Sci. Eng.* **5** E17
- [26] Delbos N *et al* 2018 LUX—A laser-plasma driven undulator beamline *Nucl. Instrum. Methods Phys. Res. A* **909** 318–22
- [27] Streeter M J V *et al* 2018 Temporal feedback control of high-intensity laser pulses to optimize ultrafast heating of atomic clusters *Appl. Phys. Lett.* **112** 24
- [28] Hooker C J *et al* 2008 Commissioning the Astra Gemini petawatt Ti: sapphire laser system *Conf. on Lasers and Electro-Optics* Optical Society of America p JThB2
- [29] Corvan D J *et al* 2014 Design of a compact spectrometer for high-flux MeV gamma-ray beams *Rev. Sci. Instrum.* **85** 065119
- [30] Leemans W P *et al* 2001 Radio-isotope production using laser-wakefield accelerators *Proc. of IPAC2001*
- [31] Carlson G *et al* 1991 A differential absorption spectrometer for determining flash x-ray spectra *Nucl. Instrum. Methods Phys. Res. B* **62** 264–74
- [32] Behm K T *et al* 2018 A spectrometer for ultrashort gamma-ray pulses with photon energies greater than 10 MeV *Rev. Sci. Instrum.* **89**
- [33] Cole J M *et al* 2018 Experimental evidence of radiation reaction in the collision of a high-intensity laser pulse with a laser-wakefield accelerated electron beam *Phys. Rev.* **8** 011020
- [34] Agostinelli S *et al* 2002 GEANT4—a simulation toolkit *Nucl. Instrum. Methods Phys. Res. A* **506** 250–303
- [35] Rusby D *et al* 2018 Novel scintillator-based x-ray spectrometer for use on high repetition laser plasma interaction experiments *Rev. Sci. Instrum.* **89** 073502
- [36] Esarey E *et al* 2009 Physics of laser-driven plasma-based electron accelerators *Rev. Mod. Phys.* **81** 1229–85
- [37] Lu W *et al* 2007 Generating multi-GeV electron bunches using single stage laser wakefield acceleration in a 3D nonlinear regime *Phys. Rev. Spec. Top.—Accel. Beams* **10** 1–12
- [38] McGuffey C *et al* 2012 Experimental laser wakefield acceleration scalings exceeding 100 TW *Phys. Plasmas* **19** 063113
- [39] Mangles S P D *et al* 2006 Laser-wakefield acceleration of monoenergetic electron beams in the first plasma-wave period *Phys. Rev. Lett.* **96** 1–4
- [40] McGuffey C *et al* 2010 Ionization induced trapping in a laser wakefield accelerator *Phys. Rev. Lett.* **104** 1–4
- [41] Schmid K *et al* 2010 Density-transition based electron injector for laser driven wakefield accelerators *Phys. Rev. Spec. Top.—Accel. Beams* **13** 1–5
- [42] Thomas A G R *et al* 2008 Monoenergetic electron beam production using dual collinear laser pulses *Phys. Rev. Lett.* **100** 16–9
- [43] Faure J *et al* 2006 Controlled injection and acceleration of electrons in plasma wakefields by colliding laser pulses *Nature* **444** 737–9
- [44] Cipiccia S *et al* 2012 A tuneable ultra-compact high-power, ultra-short pulsed, bright gamma-ray source based on bremsstrahlung radiation from laser-plasma accelerated electrons *J. Appl. Phys.* **111** 063302
- [45] Eberhard H and Werner N 2004 *The Elementary Process of Bremsstrahlung* World Scientific Lecture Notes In Physics (Singapore: World Scientific)
- [46] Li S *et al* 2017 Ultrafast multi-MeV gamma-ray beam produced by laser-accelerated electrons *Phys. Plasmas* **24** 093104
- [47] Thoms M 1996 The quantum efficiency of radiographic imaging with image plates *Nucl. Instrum. Methods Phys. Res. A* **378** 598–611
- [48] Henke B, Gullikson E and Davis J 1993 (https://henke.lbl.gov/optical_constants/)

- [49] Selwood M P *et al* 2020 Coded apertures with scatter and partial attenuation for high-energy high-resolution imaging *Plasma Phys. Control. Fusion*
- [50] Kosako K *et al* 2010 Angular distribution of bremsstrahlung from copper and tungsten targets bombarded by 18, 28 and 38MeV electrons *J. Nucl. Sci. Technol.* **47** 286–94
- [51] Saint-Gobain 2020 (www.crystals.saint-gobain.com/sites/imdf.crystals.com/files/documents/lyso-material-data-sheet.pdf)
- [52] Hubbell J and Seltzer S 2004 Nist Standard Reference Database Number 126, National Institute of Standards and Technology data retrieved in Oct 2019 (www.nist.gov/pml/x-ray-mass-attenuation-coefficients)
- [53] Rus B *et al* 2011 Outline of the eli-beamlines facility *Diode-Pumped High Energy and High Power Lasers; ELI: Ultrarelativistic Laser-Matter Interactions and Petawatt Photonics; and HiPER: the European Pathway to Laser Energy* vol 8080 (Piscataway, NJ: SPIE) p 808010
- [54] Kühn S *et al* 2017 *J. Phys. B: At. Mol. Opt. Phys.* **50**
- [55] Central Laser Facility 2020 Introducing the Extreme Photonics Applications Centre data retrieved in June 2020 (www.clf.stfc.ac.uk/Pages/EPAC-introduction-page.aspx)